Multi physics modelling for a hybrid rocket engine with liquefying fuel: a sensitivity analysis on combustion instability

Multi Physics Modelling for a Hybrid Rocket Engine with Liquefying Fuel: a Sensitivity Analysis on Combustion Instability

Lorenzo Casalino*, Andrea Ferrero†, Filippo Masseni‡, Luca Muscará§, and Dario Pastrone¶
Politecnico di Torino, Turin, 10129, Italy

Maria Luisa Frezzotti ‖, Adriano Annovazzi **, and Attilio Cretella ††
Avio S.p.A., Colleferro, 00034, Italy

Rocco Carmine Pellegrini ‡‡ and Enrico Cavallini §§
Agenzia Spaziale Italiana, Rome, 00133, Italy

Hybrid rocket engines represent a promising alternative to both solid rocket motors and liquid rocket engines. They have throttling and restart capabilities with performance similar to storable liquids, but are safer and are low-cost. However, some drawbacks, such as low regression rate and combustion instability, are limiting their effective application. Paraffin-based fuels are a solution envisaged to face the low regression rate issue, and the capability to describe and predict combustion instability in the presence of liquefying fuels becomes an enabling step towards the application of hybrid rockets in next-generation space launchers.
In this work, a multi physics model for hybrid rocket engines is presented and discussed. The model is based on a network of submodels, in which the chamber gas dynamics is described by a quasi-1D Euler model for reacting flows while thermal diffusion in the grain is described by the 1D heat equation in the radial direction. The need to introduce strong modelling simplifications introduces a significant uncertainty in the predictive capability of the numerical simulation. For this reason, a sensitivity analysis is performed in order to identify the key parameters which have the largest influence on combustion instability. Results are presented on a test case which refers to a paraffin-based grain burnt with hydrogen peroxide.

Nomenclature

A	=	cross section area
A_h	=	Arrhenius equation pre-exponential factor
A_p	=	port area
a	=	regression rate correlation coefficient
B	=	aerodynamic blowing parameter
B_t	=	thermochemical blowing parameter
C_f	=	skin friction coefficient
c_p	=	specific heat
d	=	derivative
h	=	enthalpy, thickness of liquid layer

*Full professor, Department of Mechanical and Aerospace Engineering, Corso Duca degli Abruzzi 24, 10129 Turin, Italy, AIAA Member
†Assistant Professor, Department of Mechanical and Aerospace Engineering, Corso Duca degli Abruzzi 24, 10129 Turin, Italy, AIAA Member
‡Teaching assistant, Department of Mechanical and Aerospace Engineering, Corso Duca degli Abruzzi 24, 10129 Turin, Italy, AIAA Member
§PhD student, Department of Mechanical and Aerospace Engineering, Corso Duca degli Abruzzi 24, 10129 Turin, Italy,
¶Full Professor, Department of Mechanical and Aerospace Engineering, Corso Duca degli Abruzzi 24, 10129 Turin, Italy, AIAA Associate Fellow
‖PhD Designer, Solid Propulsion Design Department, Via Degli Esplosivi 1, 0034 Colleferro, Italy
**Senior Designer, Solid Propulsioni Design Department, Via Degli Esplosivi 1, 0034 Colleferro, Italy
††Program Manager, Research Program Managment, Via Degli Esplosivi 1, 0034 Colleferro, Italy
‡‡Space Transportation, Space Infrastuctures and In-Orbit Servicing Dept., Via del Politecnico snc, 00133 Rome, Italy
§§Space Transportation, Space Infrastructures and In-Orbit Servicing Dept., Via del Politecnico snc, 00133 Rome, Italy, AIAA Senior Member

h_v	=	effective enthalpy of vaporization
E	=	total energy per unit mass
E_a	=	activation energy
e	=	internal energy per unit mass
$\boldsymbol{F}$	=	conservative fluid dynamics fluxes vector
G	=	mass flux
k_b	=	exponent of the skin friction coefficient ratio
L_m	=	latent heat of fusion
L_v	=	latent heat of vaporization
l_p	=	section perimeter
m	=	mass
N	=	number of chemical species
N_G	=	number of gaseous species
N_S	=	number of species
p	=	pressure
q	=	pre-exponential factor of the skin friction coefficient ratio
$\boldsymbol{Q}$	=	conservative fluid dynamics variables vector
$\dot{Q}$	=	heat flux
R	=	specific gas constant
R_u	=	universal gas constant
Re_x	=	local Reynolds number
$\dot{r}$	=	total regression rate
$\dot{r}_l$	=	relative liquid velocity
$\dot{r}_m$	=	regression rate of the liquid-solid interface
$\dot{r}_v$	=	evaporation regression rate
S_n	=	Swirl Number
St	=	Strouhal Number
T	=	temperature
t	=	time
u	=	axial speed
v	=	radial speed
w	=	molecular weight
x	=	axial location
Y	=	mass fraction
y	=	radial location
α	=	thermal diffusivity
α_e	=	exponential coefficient
α_g	=	gas phase absorptivity
β_e	=	exponential coefficient
γ	=	specific heats ratio
Δh	=	flame-surface enthalpy difference
Δh^0	=	enthalpy of formation
Δt	=	time step
δ	=	solid phase thermal thickness
∂	=	partial derivative
ϵ	=	mixture fraction
ϵ_g	=	gas phase emissivity
ϵ_w	=	liquid surface emissivity
λ	=	thermal conductivity
μ	=	dynamic viscosity
ρ	=	density
σ	=	Stefan-Boltzmann constant
τ	=	delay time

Superscripts

$\dot{}$	=	time derivative
n	=	n-th time step
Subscripts		
0	=	reference condition
a	=	ambient
b	=	gas flame location
bl	=	boundary layer
c	=	convective
e	=	external flow
ent	=	entrainment
F	=	fuel
g	=	grid
i	=	i-th term
int	=	interface
l	=	liquid
loc	=	local
m	=	melting
new	=	new
old	=	old
r	=	radiative
ref	=	reference value
s	=	solid
v	=	vaporization
w	=	wall
Chemical Formula		
C_2H_4	=	Ethylene
$C_{32}H_{66}$	=	paraffin wax
CO_2	=	carbon dioxide
H	=	atomic hydrogen
H_2	=	hydrogen
H_2O	=	water
H_2O_2	=	hydrogen peroxide
O	=	atomic oxygen
O_2	=	oxygen
OH	=	hydroxide

I. Introduction

Hybrid rocket engines (HREs) represent a promising alternative to both solid and liquid rocket engines. One of the most interesting advantages is related to the possibility of employing green propellants which reduce pollution and handling risks. Furthermore, the manufacturing of fuel grains is significantly less hazardous than the manufacturing of solid propellant grains in which fuel and oxidizer are mixed. Finally, HREs have throttling capabilities which allow them to share the flexibility of liquid rocket engines.

However, there are some drawbacks which prevent the widespread use of HREs. First of all, the regression rate obtained with classical fuels (high-density polyethylene, polymethilmetacrilate,...) is small and this poses severe limitations. In order to mitigate this problem, the use of liquefying fuels has been proposed and several research studies have been carried out on the behavior of these fuels [1–3]. The key phenomenon which makes liquefying fuels interesting is the so called entrainment: a layer of liquid or supercritical fuel develops on the grain surface and droplets are separated and injected in the gas because of a hydrodynamic instability. The study of liquefying fuels based on paraffin has been carried out both experimentally [2, 4–7] and numerically [8–11] and represents an active research area.

A second drawback related to HREs is represented by several mechanisms which can lead to combustion instability [12]. For these reasons, the capability to modelling combustion instabilities in HRES based on liquefying fuels represents an important goal for the further development of this technology.

In this work, a multi physics model for HREs is presented and discussed. The model is based on a network of

submodels. The chamber gasdynamics is described by a quasi-1D Euler model while thermal diffusion in the grain is described by the 1D heat equation in the radial direction. The chemical composition inside the chamber is obtained by assuming that the shifting equilibrium hypothesis holds: a surrogate model based on artificial neural networks is proposed to reduce the computational cost associated to the calculation of the equilibrium composition. Finally, some complex phenomena like entrainment and radiation are described by simple empirical models.

The need to introduce strong modelling simplifications introduces a significant uncertainty in the predictive capability of the numerical simulation. This is particularly true for the phenomena related to combustion instability. For this reason, a sensitivity analysis is performed in order to identify the key parameters which have the largest influence on combustion instability. Results are presented on a test case which refers to a paraffin-based grain burnt with hydrogen peroxide [13].

The paper is organized as follows. In Section II the physical models and the adopted discretization techniques are presented. In Section III, steady results obtained by a preliminary calibration on available reference data [13] are presented. Finally, in Section IV, unsteady results with combustion instability are presented and a sensitivity study is performed on some model coefficients characterized by a large uncertainty.

II. Multi-physics Modelling and Discretization

A. Gas-dynamic Model

The flow field in the chamber is described by the quasi-1D Euler equations augmented by a transport equation for the mixture fraction ϵ, following the approach proposed in Ref. [14].

$$\frac{\partial \mathbf{Q}A}{\partial t} + \frac{\partial \mathbf{F}A}{\partial x} = \mathbf{S}_{Q1D} + \mathbf{S}_{MASS} \tag{1}$$

$$\mathbf{Q} = (\rho, \rho u, \rho E, \rho\epsilon)^T \tag{2}$$

$$\mathbf{F} = \left(\rho u, p + \rho u^2, u(p + \rho E), rhou\epsilon\right)^T \tag{3}$$

$$\mathbf{S}_{Q1D} = \left(0, p\frac{\partial A}{\partial x}, 0, 0\right)^T \tag{4}$$

$$\mathbf{S}_{MASS} = \left(\dot{m}_F l_p, 0, \dot{m}_F l_p h_w, \dot{m}_F l_p\right)^T \tag{5}$$

where ρ, p, E, u, ϵ, l_p, A_p represent density, pressure, total energy per unit mass, speed, mixture fraction, section perimeter and port area, respectively. The variables $\dot{m}_F$ and h_w refer to the fuel flux emitted by the grain and the related enthalpy. The mixture fraction ϵ is defined according to [14]:

$$\epsilon = \frac{b_C - b_{C,2}}{b_{C,1} - b_{C,2}} \tag{6}$$

where b_C is the mole number of atomic element C per unit mass of mixture gas and 1 and 2 represent the fuel and oxidizer stream, respectively. Total energy per unit mass E and the internal energy per unit mass are evaluated for a mixture with N chemical species as:

$$E = e + \frac{u^2}{2} \tag{7}$$

$$e = \sum_{i=1}^{N} h_i Y_i - \frac{p}{\rho} \tag{8}$$

$$h_i = \Delta h_i^0 + \int_{T_0}^{T} c_{p,i} dT \tag{9}$$

where h_i, Y_i, Δh_i^0, $c_{p,i}$ represent enthalpy, mass fraction, enthalpy of formation and specific heat, respectively. The specific heat is expressed as a polynomial fitting of temperature. Finally, the ideal gas law is assumed for all the simulated species:

$$p = \sum_{i=1}^{N} \frac{Y_i}{w_i} \rho R_u T = \rho R T \tag{10}$$

The governing equations are discretized by means of the method of lines. A second order accurate finite volume method is chosen for space discretization. The reconstruction is limited by means of the minmod limiter and the fluxes at the interfaces are computed by means of the AUSM+ numerical flux [15]. Time integration is performed by means of a second order accurate Runge-Kutta scheme.

B. Thermal Model

The source term represented by Eq. 5 in the gas dynamic model requires to model the grain regression rate. This can be done by considering the 1D heat equation in the radial direction. In this work a liquefying fuel represented by a paraffin wax is considered: as a result, the heat equation must be solved in the solid grain and in the liquid layer which covers the grain. Since the gas dynamic model is described by the quasi-1D Euler equations discretized along the axial direction, the equations of the thermal model are solved for each cell of the gas dynamic domain: axial conduction in the grain is neglected.
The two equations of the thermal model written in a reference system which follows the liquid-gas interface are defined according to Barato et al. [16]:

$$\frac{\partial T}{\partial t} = \dot{r}_l \frac{\partial T}{\partial y} + \alpha_l \frac{\partial^2 T}{\partial y^2} \tag{11}$$

$$\frac{\partial T}{\partial t} = \dot{r} \frac{\partial T}{\partial y} + \alpha_s \frac{\partial^2 T}{\partial y^2} \tag{12}$$

In the equations above, the relative liquid velocity $\dot{r}_l$ can be expressed as the following:

$$\dot{r}_l = v_l + \dot{r} = \dot{r}_m \left(\frac{\rho_s}{\rho_l} - 1 \right) + \dot{r} = \frac{\dot{m}_F}{\rho_l} \tag{13}$$

where the different phase density is taken into account through a mass balance over the liquid-solid interface. The total fuel mass flux can be expressed as a sum of two terms ($\dot{m}_F$=$\dot{m}_v$+$\dot{m}_{ent}$), the vaporization mass flux and the fuel mass flux due to the entrainment mechanism. Regarding the vaporization mass flux the following expression is used:

$$\dot{m}_v = \rho_s \dot{r}_v \tag{14}$$

In this work, the $C_{32}H_{66}$ paraffin wax is considered. According to Karabeyoglu et al. [17], the critical pressure for $C_{32}H_{66}$ is approximately 5 atm and, as a consequence, the chamber pressure is above the critical pressure in the typical operating conditions of a HRE. Since the flow in the melted layer is in supercritical condition, the surface phenomena are driven by the pyrolysis process and the evaporation regression rate is evaluated as the following:

$$\dot{r}_v = A_h e^{-\frac{E_a}{RT_w}} \tag{15}$$

The fuel mass flux originated by the entrainment mechanism is evaluated with the equation below.

$$\dot{m}_{ent} = \rho_s \dot{r}_{ent} \tag{16}$$

The entrainment regression rate $\dot{r}_{ent}$ depends on the total regression rate through the total mass flux according to Karabeyoglu et al. [17].

$$\dot{r}_{ent} = \frac{a_{ent} G^{2\alpha}}{\dot{r}^{\beta}} \tag{17}$$

In the equation above a_{ent} is the entrainment coefficient, which is function of the fuel property and the values for the exponential coefficients are $\alpha_e = 1.5$ and $\beta_e = 2$ as it was shown in [17]. In addition, the liquid-layer thickness dynamics is taken into account with the following expression:

$$\frac{dh}{dt} = \dot{r}_m - \dot{r} \tag{18}$$

As far as boundary conditions are concerned, the total heat flux at the gas-liquid (or supercritical fluid) interface has to be equal to the conductive heat transfer into the liquid (or supercritical fluid) and the heat needed for the phase transformation.

$$\dot{Q}_{tot} = \dot{m}_v L_v - \lambda_l \left.\frac{\partial T}{\partial y}\right|_{y=0} \tag{19}$$

In Eq. 19, the total heat flux is the sum of the convective and the radiative heat flux ($Q_{tot} = Q_c + Q_r$). The boundary condition at the liquid-solid interface is expressed as the following:

$$T|_{y=h} = T_m \tag{20}$$

$$-\lambda_l \left.\frac{\partial T}{\partial y}\right|_{y=h^-} + \lambda_s \left.\frac{\partial T}{\partial y}\right|_{y=h^+} = L_m \rho_s \dot{r}_m \tag{21}$$

Finally, the ambient temperature T_a is imposed on the boundary domain deep in the solid grain.

The equations 11 and 12 must be solved on a dynamic mesh due to the liquid-layer thickness dynamics. For this reason, it is necessary to take special attention of the mesh construction, the discretization of the convective flux term and the numerical time integration. The spatial discretization is obtained by using the finite volume method, where the diffusive flux term is discretized with a second order central scheme and the convective flux term with the second order upwind scheme through the minmod slope limiter. The time integration is performed with the second order Runge-Kutta SSP (Strong Stability Preserving) [18]. The time integration scheme must consider the time evolving grid deformation; consequently, it has followed the approach suggested in [19]. The mesh grid is discretized with 100 cells 20 of which are in the liquid phase. The grid nodes are uniformly spaced from the liquid layer to the first grid node after the liquid-solid interface; after this point, the grid nodes in the solid layer are drown with a geometric progression in order to have the location of the last grid node at 100δ, where $\delta = \frac{\alpha_s}{\dot{r}_{ref}}$ is the thermal thickness in the solid phase.

C. Convective Heat Flux Modelling

Assuming a fully developed turbulent boundary layer inside the combustion chamber and the validity of the Reynolds analogy in the quasi-stationary condition, the following expression for the convective heat flux can be assumed according to Karabeyoglu [20]:

$$\dot{Q}_c = \frac{1}{2} C_f G \left(\frac{u_e}{u_b}\right) \Delta h \tag{22}$$

The convective heat flux through the boundary layer is limited by the blowing of the gasified fuel. This phenomenon is taken into account by the introduction of the aerodynamic blowing parameter evaluated as the following:

$$B = \frac{2\rho_F \dot{r}_v}{G C_f} \tag{23}$$

According to Karabeyoglu et al. [20], the vaporization of the fuel particle detached from the liquid surface takes place above the flame sheet; on account of that, the evaporation regression rate appears in the above equation instead of the total regression rate. The skin friction coefficient is estimated by following the approach of Pastrone and Carmicino in [21]. Accordingly, in the range $5 \geq B \geq 100$ the ratio between the skin friction coefficient affected by blowing and the skin friction without blowing is expressed as follows:

$$\frac{C_f}{C_{f0}} = q B^{-k_b} \tag{24}$$

In the case where $B \rightarrow 0$ the ratio of the skin friction coefficients is estimated differently with the following equation:

$$\frac{C_f}{C_{f0}} = \frac{1}{1+0.4B} \tag{25}$$

The two equations above match each other by imposing $q = 0.996$ and $k_b = 0.68$ if $B = B_{ref} = 5.313$. The skin friction coefficient without blowing is estimated according to the correlation reported in [20].

Eventually, by taking into account the thermochemical blowing parameter $B_t = \left(\frac{u_e}{u_b}\right)\frac{\Delta h}{h_v}$, the following two expressions for the convective heat flux can be derived.

$$\dot{Q}_c = B_t h_v \left(\frac{1}{2}C_{f0}G - 0.4\rho_F \dot{r}_v\right) \quad \text{if} \quad B \leq B_{ref} \tag{26}$$

$$\dot{Q}_c = \frac{0.996}{2}C_{f0}B_t h_v \left(\frac{2\rho_F \dot{r}_v}{0.996GC_{f0}}\right)^{\frac{-k_b}{1-k_b}} \quad \text{if} \quad B > B_{ref} \tag{27}$$

D. Boundary Layer Delay Modelling

The combustion instability in a HRE, according to [22], depends on three physical phenomena: the blocking-effect due to the blowing of the fuel gas, the thermal transient and the boundary layer delay time. The instability can be introduced in the model by defining a characteristic time that represents the boundary layer delay time. This parameter can be estimated as a function of the Reynolds number according to [22]:

$$\tau_{bl} = 2.18{Re_x}^{-0.1}\frac{x}{u_e} \tag{28}$$

E. Radiative Heat Flux

In the boundary condition at the liquid-gas interface the total heat flux is the sum of convective and radiative heat flux. The radiative heat transfer does not influence strongly the regression rate but it could become important when considering fuels with metal additives or sooting fuels. Empirical relations are available to the estimation of the radiative heat flux [12, 23]:

$$\dot{Q}_r = \sigma\epsilon_w\left(\epsilon_g {T_b}^4 - \alpha_g {T_w}^4\right) \tag{29}$$

Since the flame temperature is significantly higher than the surface temperature and, in addition, the gas phase emissivity and absorptivity are of the same order, the equation for the radiative heat transfer can be approximated as the following:

$$\dot{Q}_r = \sigma\epsilon_w\epsilon_g {T_b}^4 \tag{30}$$

F. Swirl Model

The use of swirl injectors can significantly increase the regression rate by improving convective heat transfer. In order to model the use of a swirl injector, an empirical correction is introduced. The gas dynamic model considered in this work is quasi-1D: this means that it can describe only the axial component of the velocity. In order to introduce the swirl effect, a correction factor is introduced on the gas velocity in order to keep into account the tangential velocity component. As a result, also the characteristic boundary layer delay is corrected. According to [24], the swirl number S_n is defined as

$$S_n = \frac{2}{3}\frac{v}{u} \tag{31}$$

where v and u represent the tangential and axial velocity components. The swirl correction factor K is computed as

$$K = \sqrt{1 + (\frac{3}{2}S_n)^2} \tag{32}$$

The factor K allows to correct the axial mass flux and speed by computing some equivalent values which take into account the swirl and allow to obtain an increased convective flux. In this strong approximation, S_n represents the

average swirl number in the combustion chamber. Furthermore, in this approach the particles should move in a spiral trajectory: for this reason, the correction factor K is applied also to the space coordinate which appears in the empirical relation used to compute the skin friction coefficient C_f.

G. Chemical Model

In the combustion chamber of a HRE the characteristic time related to fluid dynamics phenomena is remarkably higher than the characteristic time associated to chemical reactions. For this reason, it is reasonable to assume that the shifting equilibrium hypothesis holds. This assumption is in line with the approach proposed by Karthikeyan and Shimada in Ref. [14] and applied to the modeling of the combustion chamber of HREs.

In the present work, the chemical equilibrium is computed by means of two different approaches, namely a high fidelity and a surrogate model. The High Fidelity Model (HFM) is based on the NASA CEA (Chemical Equilibrium with Applications) code (see Subsection 1) [25]. Such an approach, however, is really demanding in terms of computational time when embedded in the fluid dynamic solver which requires to compute the equilibrium composition in each cell at each time step. For this reason, Karthikeyan and Shimada in Ref. [14] proposed to freeze the molar fractions of the chemical species for a certain number of time steps. Nevertheless, this approach is in contrast with the initial assumption concerning the characteristic times of fluid dynamics and chemical reactions. Hence, in the present work, the authors opt for the introduction of a surrogate chemical model, able to compute the chemical composition in each cell at each time step, but at an affordable computational cost. Such surrogate model is depicted in Subsection 2.

The evaluation of the chemical composition in equilibrium conditions is usually based on Gibbs' free energy minimization principle (when pressure and temperature of the reactions are given) or on Helmholtz's free energy minimization principle (when density and internal energy are given). In the present approach, the conservation principles employed in the gas-dynamic model describe the evolution of mass, momentum and energy. Thus, the chemical composition in equilibrium conditions can be easily computed minimizing Helmholtz free energy. For this reason, the inputs of the chemical model are density, internal energy and the the local mixture ratio ϵ. The outputs are the mole fractions of the combustion products and the ratio of the specific heats γ.

1. High Fidelity Model

The HFM assumes that all the gaseous chemical species present in the combustion chamber can be regarded as ideal gases and that their mixture follows the ideal gas equation as well. In this context, N_S stands for the number of chemical species in the mixture, whereas N_G is the number of gaseous species. The chemical equilibrium problem is solved minimizing the Helmholtz free energy by means of the approach proposed by McBride and Gordon, whose details can be found in Ref. [25] and are here only summarized.

The free energy equation is written as a function of the molar internal energy and entropy, whereas mass balances between reactants and products provide a set of constraints which are introduced through the method of the Lagrange multipliers. The system of equations which arises is non-linear and can be numerically solved by means of Newton-Raphson's method. Once the molar concentrations are know, the molecular weight of the mixture can be computed.

In the present work, the breakdown products of a paraffin-based wax are considered as fuels, i.e. ethylene and hydrogen. Hydrogen Peroxide (HP) is considered as oxidizer. The following species are considered in the model: CO_2, C_2H_4, H, H_2, H_2O, O, OH, O_2, H_2O_2.

2. Surrogate Model

In order to reduce the computational cost required by the chemical equilibrium problem, an Artificial Neural Network (ANN) surrogate chemical model is developed. The ANN requires three inputs, namely internal energy, density and local mixture ratio, whereas the output parameters are the molar fractions of the combustion products and the ratio of the specific heats γ. An example of the employed ANN architecture is reported in Fig. 1, where it is possible to identify the three inputs (on the left), two hidden layers of ten neurons each and the output layer of ten outputs (on the right). The architecture was chosen in a preliminary study as a trade-off between prediction accuracy and training/prediction cost.

The ANN is trained in Matlab and embedded into a Fortran 90 code which solves the gas dynamic equations. The training database is generated varying the input parameters between their minimum and maximum values obtained in some preliminary runs of the solver with the high-fidelity model. Initially, a uniform sampling was used for the generation of the training database with the high-fidelity model. However, some of these training points lead to

unfeasible solutions (i.e. the high fidelity model is unable to find a physical solution) and thus have been discarded from the training database.

The training has been performed by means of the Levenberg-Marquardt algorithm, which aims at the minimization of the mean square error between the reference data set and the ANN reconstruction. The database is split into a training database (75% of the trials), a validation database (15% of the trials) and a test database (10% of the trials). The trials in the training database are used to determine the merit function (i.e. the mean square error on the fitting) which drives the training process. The validation trials are not used within the training but to stop it when the over-fitting issue kicks in. In the end, the test trials are not exploited during the training process but they are used a-posteriori in order to evaluate the ANN prediction capabilities.

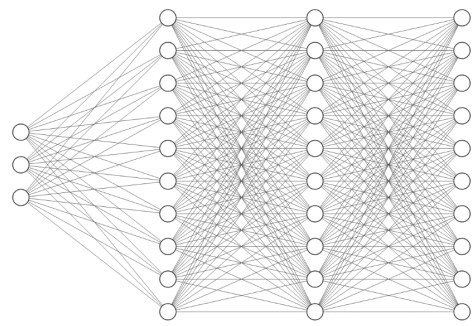

Fig. 1 ANN architecture used in the surrogate chemical model.

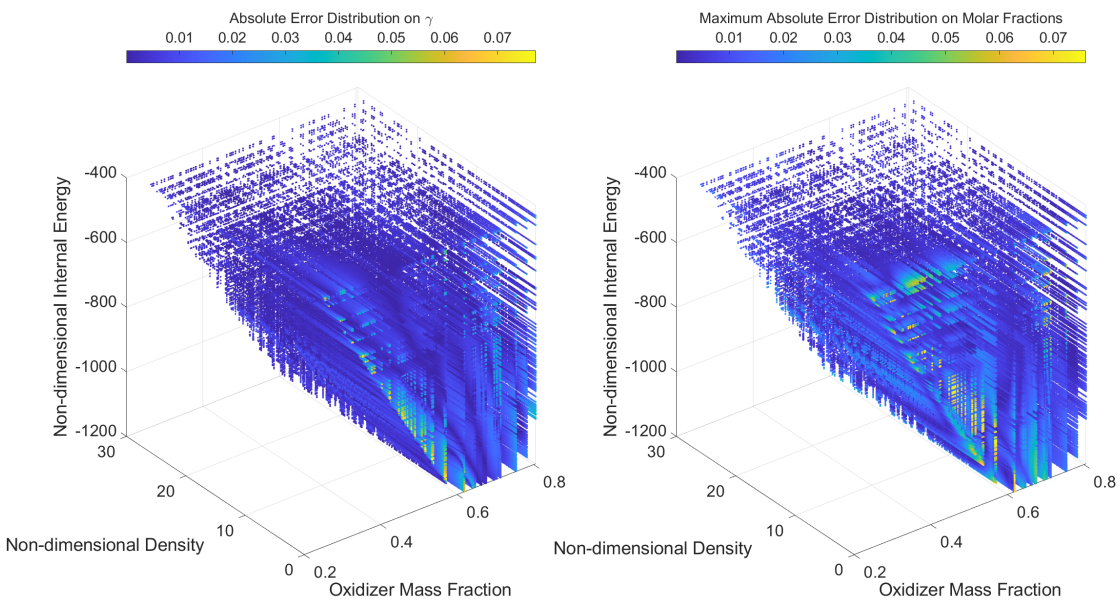

Fig. 2 Absolute error distribution on γ and maximum absolute error distribution on molar fractions between HFM and surrogate model.

In order to further check the performance of the ANN, a large test database obtained by random sampling on the training range is considered. The results of this test are reported in Fig. 2 for a training database made of 10^6 points. The plot on the left reports the absolute error distribution on the value of γ, obtained by the ANN with respect to the HFM. In the same way, the plot on the right shows the maximum absolute error among all the products molar fractions for each point of the database. The axes of both diagram reports the non-dimensional internal energy, non-dimensional density and oxidizer mass fraction in the reagents mixture. The relative errors are smaller than 1% for both γ and the molar fractions, with the exception of the low density region, which however is not relevant for the typical operating condition of the hybrid rocket engines considered in the present analysis (light blue and yellow points in Fig. 2). Thus, the proposed surrogate model has been used in place of the HFM in the followings, grating a relevant reduction in the computational cost of the simulations.

III. Steady Results

First of all, the model is calibrated in steady state conditions by considering an engine burning paraffin and hydrogen peroxide (90% concentration) which was experimentally tested by [13]. The steady results are obtained by setting the boundary layer delay τ_{bl} to zero. Among the different configurations described in the experimental work [13], the selected one is characterized by the largest O/F ratio: 4.03.

The computational domain considered in the gas dynamics module includes the pre-chamber ($0 \leq x/L_{ref} \leq 0.1$), the grain section ($0.1 \leq x/L_{ref} \leq 0.8$) and the nozzle ($x/L_{ref} > 0.8$): the domain ends after the nozzle throat in order to achieve supersonic exit boundary conditions. In all the plots reported in this work, the axial position is normalized with respect to the total length of the computational domain ($L_{ref} = 0.243$ m).

The port area and the pre-chamber area are set equal to the same value, obtained by considering the average port area during the combustion ($A_p = 1.25 \cdot 10^{-3} m^2$). The throat area A_t is set to $7.125 \cdot 10^{-5} m^2$ and the throat is located at $x/L_{ref} = 0.925$.

The calibration is performed by optimizing the values of the coefficients a_{ent} and A_h in order to match the experimental average regression rate. Starting from data available in the literature, the following values were determined: $a^*_{ent} = 1.26 \cdot 10^{-13} m^9/kg^3$, $A^*_h = 1.88 \cdot 10^7 m/s$. Radiative effects are not considered in this simulation. As a result, the average regression rate is obtained equal to 2.71 mm/s which is in line with the experimental reference value (2.65 mm/s).

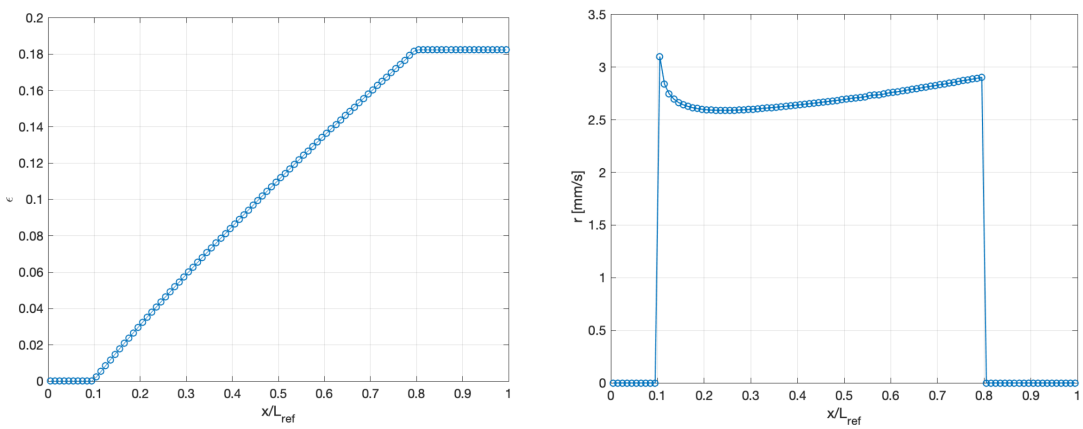

(a) (b)

Fig. 3 Mixture fraction ϵ (a) and regression rate r (b) along the grain axis for the steady solution.

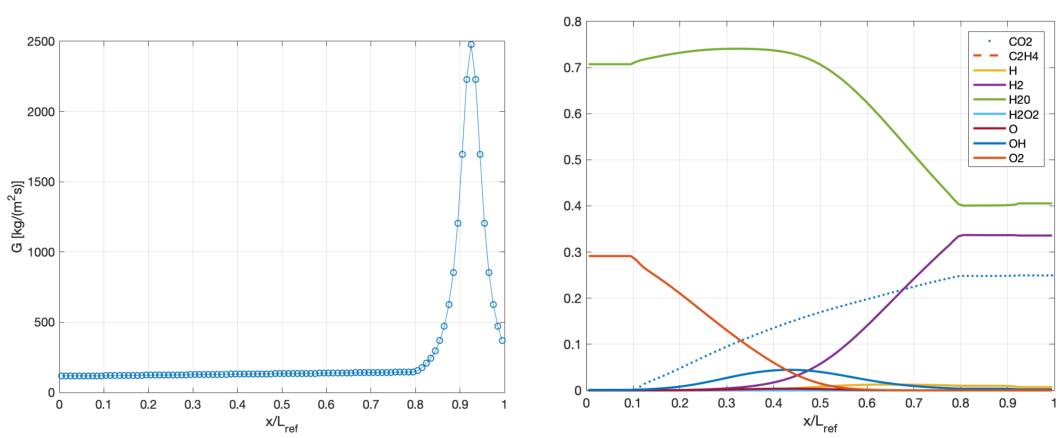

(a) (b)

Fig. 4 Mass flux G (a) and combustion products molar fractions along the grain axis for the steady solution.

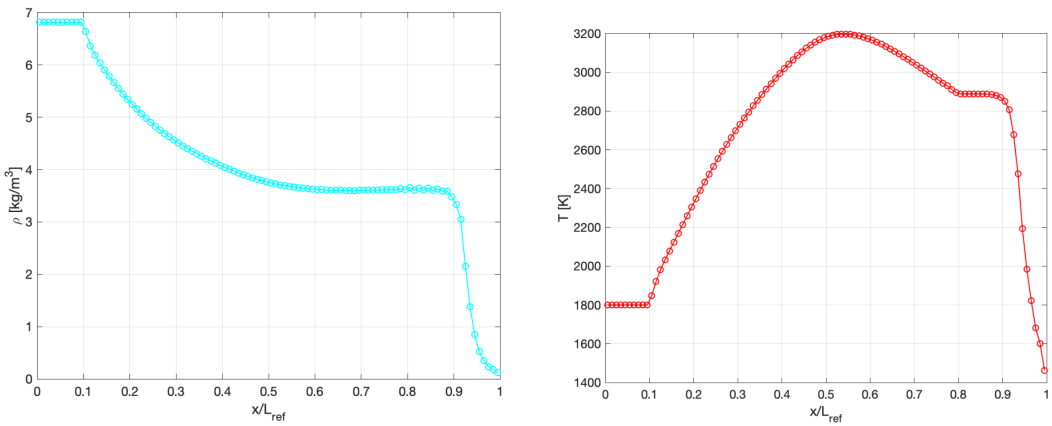

(a) (b)

Fig. 5 Density ρ (a) and temperature T (b) along the grain axis for the steady solution.

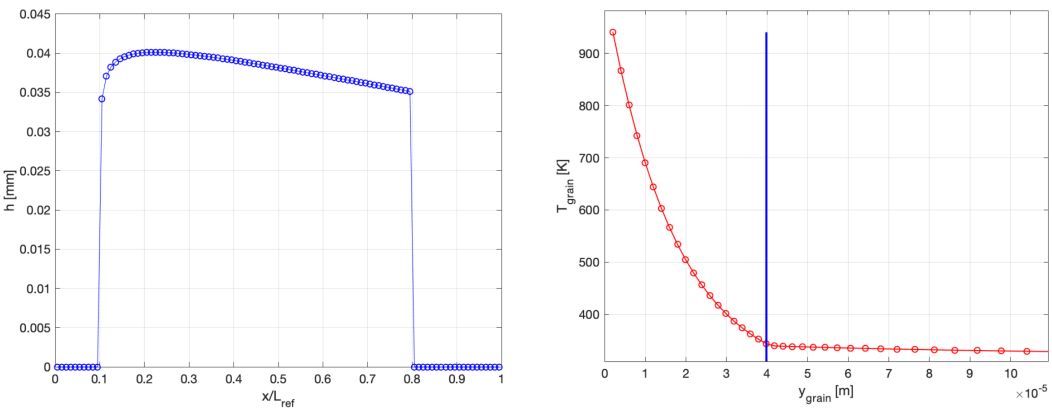

(a) (b)

Fig. 6 Liquid layer thickness h (a) along the grain axis and grain temperature T_{grain} within the grain thickness for the steady solution.

IV. Unsteady Results

The results obtained by the steady simulation (Case A, in the following) represent a baseline solution which will be considered as reference in the following of the study. A set of unsteady simulations is performed in order to evaluate the effects of some model coefficients. This sensitivity analysis is focused on four target quantities: average chamber pressure $\bar{p}_c$, relative mean squared pressure fluctuation $\Delta p_2\%$, relative peak-to-peak pressure fluctuation $\Delta p_{pp}\%$ and average regression rate $\bar{r}$. The average quantities are obtained by performing time averaging on the statistically steady solution obtained after the initial transient. In particular, the impact of the following coefficients is investigated: boundary layer delay τ_{bl}, entrainment coefficient a_{ent}, Arrhenius pre-exponential coefficient A_h, overall radiative coefficient $\epsilon_g \epsilon_w$, swirl number S_n. The results of the simulations (A-G) and the corresponding set of coefficients are summarized in Table 1.

First of all, an unsteady simulation with a uniform boundary layer delay (Case B) is performed (τ_{bl} = 5 ms). The obtained pressure spectrum is reported in Figure 7. The first peak is in good agreement with the fundamental hybrid frequency predicted according to the Karabeyoglu correlation [22], $f = 0.48/\tau_{bl} = 96$ Hz . It is interesting to note that the instability induces a significant increase in the average chamber pressure and regression rate (DC shift phenomenon).

All the other simulations are performed by imposing an axial distribution of $\tau_{bl} = f(x)$ obtained by applying Eq. 28 to the previously computed steady state solution. A plot of this distribution is reported in Figure 8a. This is a better approximation with respect to the imposition of a uniform boundary layer delay. Ideally, it could be possible to apply

Table 1 Sensitivity analysis.

Case	τ_{bl} [ms]	a_{ent}	A_h	$\epsilon_g\epsilon_w$	S_n	$\bar{p}_c$ [bar]	Δp_2%	Δp_{pp}%	r [mm/s]
A	0	a^*_{ent}	A^*_h	0.00	0.00	46.18	0.00	0.00	2.71
B	$\tau_{bl}(x) = 5$ ms	a^*_{ent}	A^*_h	0.00	0.00	47.35	0.87	4.10	3.21
C	$\tau_{bl}(x) = f(x)$	a^*_{ent}	A^*_h	0.00	0.00	47.36	0.75	5.09	3.22
D	$\tau_{bl}(x) = f(x)$	$2a^*_{ent}$	A^*_h	0.00	0.00	48.35	0.54	3.74	3.81
E	$\tau_{bl}(x) = f(x)$	a^*_{ent}	$2A^*_h$	0.00	0.00	47.54	0.86	5.55	3.33
F	$\tau_{bl}(x) = f(x)$	a^*_{ent}	A^*_h	0.04	0.00	47.47	0.89	6.32	3.29
G	$\tau_{bl}(x) = f(x)$	a^*_{ent}	A^*_h	0.00	1.00	50.23	0.43	2.44	6.16

Eq. 28 at run-time in the unsteady simulation in order to get a delay which varies both in space and in time, according to the local state of the boundary layer. However, Eq. 28 is valid only for a steady solution and its application to the unsteady solution could lead to nonphysical results, for example when the flow inverts its direction during the strong initial transient. The pressure spectrum obtained by setting $\tau_{bl} = f(x)$ and keeping the original values for all the other coefficients (Case C) is reported in Figure 7b: it is no more possible to identify a clear set of peaks because in this simulation the boundary layer delay varies continuously along the axial direction. Also in this case it is possible to observe a significant DC shift.

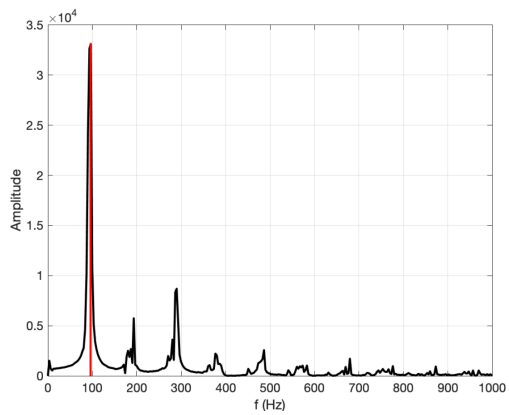

Fig. 7 Pressure spectrum for unsteady combustion with uniform boundary layer delay (τ_{bl}=5 ms).

In Case D, the effect of entrainment is investigated by doubling the coefficient a_{ent} with respect to the value obtained by the calibration (a^*_{ent}). As a result, average regression rate and chamber pressure are increased with respect to case C. Furthermore, the increased entrainment leads to some benefits on the combustion instability: both Δp_2% and Δp_{pp}% are reduced with respect to the Case C.

In case E, the effect of vaporization and pyrolysis is investigated by doubling the Arrhenius coefficient A_h with respect to the value obtained by the calibration (A^*_h). Also in this case, the average regression rate and chamber pressure are increased with respect to Case C. However, the pressure oscillations, quantified by the coefficients Δp_2% and Δp_{pp}% remain comparable to what observed in the Case C.

In Case F, the effect of radiative fluxes is evaluated by setting the overall radiative coefficient as $\epsilon_g\epsilon_w = 0.04$. This tentative value was chosen after some tests in order to keep the radiative flux below 10% of the convective flux, as reported in the literature [12]. The results show that the radiative flux leads to an increase in the average regression rate, chamber pressure and pressure fluctuations with respect to the Case C.

Finally, in case G the effects of swirl injection are estimated. In particular, the swirl number is set to $S_n = 1$. This leads to a strong increase in the average regression rate and chamber pressure. Furthermore, the swirl has an important

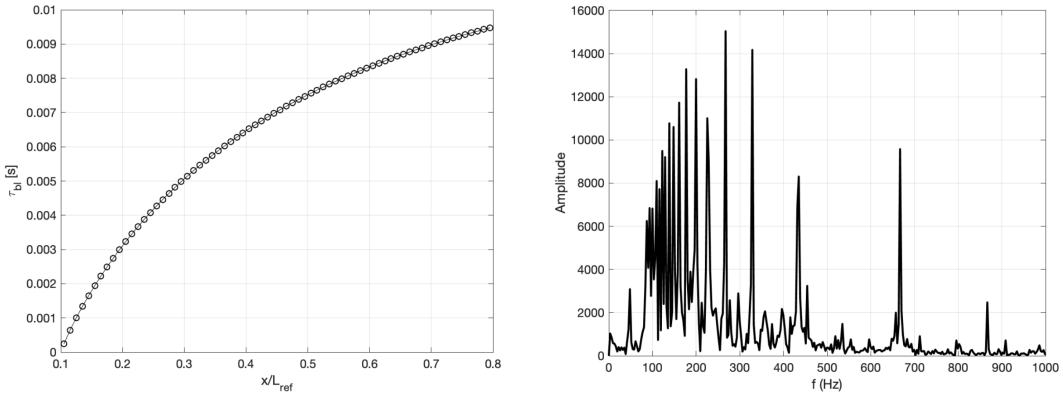

(a) (b)

Fig. 8 Boundary layer delay estimated from the steady solution (a) and pressure spectrum obtained by imposing this delay distribution.

effect on the instability: both Δp_2% and Δp_{pp}% are significantly reduced with respect to Case C.

V. Conclusions

A multi physics model for the prediction of the unsteady flow field in a HRE with liquefying fuel is presented. The model has a relatively low computational cost since it is based on a quasi-1D Euler solver coupled with a 1D thermal solver. In order to further reduce the computational cost, a surrogate model based on a ANN is adopted to compute the equilibrium chemical composition. As a result, the model can be adopted in the design process of a HRE in order to identify the risk of instability. The complexity of the involved physical phenomena requires severe simplifications in several problems which are approximated by empirical relations. This introduces a significant uncertainty on the predicted results and on the definition of the model parameters. For this reason, a sensitivity analysis was performed in order to identify the impact of some key parameters on regression rate and instability. The parametric study provides some guidelines which can be adopted during the design process. In particular, the results show that an increase in the entrainment phenomenon increases the regression rate but has a beneficial effect on the instability. This suggests the use of paraffin based fuel with a reduced amount of additives in order to maximize the entrainment phenomenon: however, it is necessary to take into account also the mechanical properties of the fuel grain, which are not considered in this work and which can benefit from the introduction of additives in the composition.
Finally, a simple empirical correction for the presence of a swirled flow is introduced: the results suggest that the swirl allows to significantly increase the regression rate while limiting the combustion instability. This numerical result is in line with previous experimental findings reported by [26].

VI. Acknowledgment

This work is performed under the funding of the Italian Space Agency contract n. 2019-5-I.0 CUP n. F84E16002240003 related to R&D on hybrid propulsion.

References

[1] Karabeyoglu, M., Altman, D., and Cantwell, B., "Combustion of Liquefying Hybrid Propellants: Part 1, General Theory," *Journal of Propulsion and Power*, Vol. 18, No. 3, 2002, pp. 610–620. doi:10.2514/2.5975.

[2] Karabeyoglu, A., Zilliac, G., Cantwell, B. J., DeZilwa, S., and Castellucci, P., "Scale-up Tests of High Regression Rate Paraffin-based Hybrid Rocket Fuels," *Journal of propulsion and power*, Vol. 20, No. 6, 2004, pp. 1037–1045. doi:10.2514/1.3340.

[3] Karabeyoglu, M., and Cantwell, B. J., "Combustion of Liquefying Hybrid Propellants: Part 2, Stability of Liquid Films," *Journal of Propulsion and Power*, Vol. 18, No. 3, 2002, pp. 621–630. doi:10.2514/2.5976.

[4] Paravan, C., Galfetti, L., Bisin, R., and Piscaglia, F., "Combustion Processes in Hybrid Rockets," *International Journal of Energetic Materials and Chemical Propulsion*, Vol. 18, No. 3, 2019. doi:10.1615/IntJEnergeticMaterialsChemProp.2019027834.

[5] Di Martino, G., Mungiguerra, S., Carmicino, C., Savino, R., Cardillo, D., Battista, F., Invigorito, M., and Elia, G., "Two-hundred-newton laboratory-scale hybrid rocket testing for paraffin fuel-performance characterization," *Journal of Propulsion and Power*, Vol. 35, No. 1, 2019, pp. 224–235.

[6] Bouziane, M., Bertoldi, A., Hendrick, P., and Lefebvre, M., "Experimental Investigation of the Axial Oxidizer Injectors Geometry on a 1-kN Paraffin-Fueled Hybrid Rocket Motor," *FirePhysChem*, 2021. doi:10.1016/j.fpc.2021.11.012.

[7] Thomas, J. C., Paravan, C., Stahl, J. M., Tykol, A. J., Rodriguez, F. A., Galfetti, L., and Petersen, E. L., "Experimental Evaluation of HTPB/paraffin Fuel Blends for Hybrid Rocket Applications," *Combustion and Flame*, Vol. 229, 2021, p. 111386. doi:10.1016/j.combustflame.2021.02.032.

[8] Bellomo, N., Barato, F., Faenza, M., Lazzarin, M., Bettella, A., and Pavarin, D., "Numerical and Experimental Investigation of Unidirectional Vortex Injection in Hybrid Rocket Engines," *Journal of Propulsion and Power*, Vol. 29, No. 5, 2013, pp. 1097–1113. doi:10.2514/1.B34506.

[9] Ranuzzi, G., Cardillo, D., and Invigorito, M., "Numerical Investigation of a N2O-paraffin Hybrid Rocket Engine Combusting Flowfield," *6th european conference for aeronautics and space sciences (EUCASS)*, EUCASS Rhode-St-Genese, Belgium, 2015. doi:10.13140/RG.2.1.1329.6727.

[10] Lazzarin, M., Faenza, M., Barato, F., Bellomo, N., Bettella, A., and Pavarin, D., "Computational Fluid Dynamics Simulation of Hybrid Rockets of Different Scales," *Journal of Propulsion and Power*, Vol. 31, No. 5, 2015, pp. 1458–1469. doi: 10.2514/1.B35528.

[11] Leccese, G., Bianchi, D., and Nasuti, F., "Modeling and Simulation of Paraffin–Based Hybrid Rocket Internal Ballistics," *2018 Joint Propulsion Conference*, 2018, p. 4533. doi:10.2514/6.2018-4533.

[12] Kuo, K. K., and Chiaverini, M. J., *Fundamentals of Hybrid Rocket Combustion and Propulsion*, American Institute of Aeronautics and Astronautics, 2007. doi:10.2514/4.866876.

[13] Brown, T. R., and Lydon, M. C., "Testing of Paraffin-Based Hybrid Rocket Fuel Using Hydrogen Peroxide Oxidizer," *AIAA Region 5 Student Conference, Wichita, USA*, 2005.

[14] Karthikeyan, G., and Shimada, T., "Numerical Parametric Analysis of Combustion Instability in Axial-injected Hybrid Rocket Motors," *Journal of Propulsion and Power*, Vol. 34, No. 6, 2018, pp. 1542–1552. doi:10.2514/1.B36826.

[15] Liou, M.-S., "A Sequel to Ausm: Ausm+," *Journal of computational Physics*, Vol. 129, No. 2, 1996, pp. 364–382. doi: 10.1006/jcph.1996.0256.

[16] Barato, F., Bellomo, N., Faenza, M., Lazzarin, M., Bettella, A., and Pavarin, D., "Numerical Model to Analyze Transient Behavior and Instabilities on Hybrid Rocket Motors," *Journal of Propulsion and Power*, Vol. 31, No. 2, 2015, pp. 643–653. doi:10.2514/1.B35282.

[17] Karabeyoglu, A., Cantwell, B., and Stevens, J., "Evaluation of the Homologous Series of Normal Alkanes as Hybrid Rocket Fuels," *41st AIAA/ASME/SAE/ASEE Joint Propulsion Conference & Exhibit*, 2005, p. 3908. doi:10.2514/6.2005-3908.

[18] Gottlieb, S., and Shu, C.-W., "Total Variation Diminishing Runge-Kutta Schemes," *Mathematics of computation*, Vol. 67, No. 221, 1998, pp. 73–85. doi:10.1090/S0025-5718-98-00913-2.

[19] Batina, J. T., "Unsteady Euler Airfoil Solutions Using Unstructured Dynamic Meshes," *AIAA journal*, Vol. 28, No. 8, 1990, pp. 1381–1388. doi:10.2514/3.25229.

[20] Karabeyoglu, M. A., and Altman, D., "Dynamic Modeling of Hybrid Rocket Combustion," *Journal of Propulsion and Power*, Vol. 15, No. 4, 1999, pp. 562–571. doi:10.2514/2.5464.

[21] Carmicino, C., and Pastrone, D., "On the Explanation of the "DC Shift" in Hybrid Rockets," *2018 Joint Propulsion Conference*, 2018, p. 4525. doi:10.2514/6.2018-4525.

[22] Karabeyoglu, M. A., De Zilwa, S., Cantwell, B., and Zilliac, G., "Modeling of Hybrid Rocket Low Frequency Instabilities," *Journal of Propulsion and Power*, Vol. 21, No. 6, 2005, pp. 1107–1116. doi:10.2514/1.7792.

[23] Marxman, G., Wooldridge, C., and Muzzy, R., "Fundamentals of Hybrid Boundary-layer Combustion," *Progress in Astronautics and Rocketry*, Vol. 15, Elsevier, 1964, pp. 485–522. doi:10.1016/B978-1-4832-2730-6.50025-7.

[24] Greatrix, D. R., "Geometric Swirl Number and Hybrid Rocket Engine Performance," *2018 Joint Propulsion Conference*, 2018, p. 4442. doi:10.2514/6.2018-4442.

[25] McBride, B. J., *Computer Program for Calculation of Complex Chemical Equilibrium Compositions and Applications*, Vol. 2, NASA Lewis Research Center, 1996.

[26] Bellomo, N., Faenza, M., Barato, F., Bettella, A., Pavarin, D., and Selmo, A., "The" Vortex Reloaded" Project: Experimental Investigation on Fully Tangential Vortex Injection in N2O-paraffin Hybrid Motors," *48th AIAA/ASME/SAE/ASEE Joint Propulsion Conference & Exhibit*, 2012, p. 4304. doi:10.2514/6.2012-4304.